

Primordial Earth mantle heterogeneity caused by the Moon-forming giant impact

Hongping Deng¹, Maxim D. Ballmer², Christian Reinhardt¹, Matthias M. M. Meier³, Lucio Mayer¹, Joachim Stadel¹, Federico Benitez¹

¹*Center for theoretical Astrophysics and Cosmology, Institute for Computational Science, University of Zurich, Winterthurerstrasse 190, 8057 Zurich, Switzerland*

²*Institute of Geophysics, ETH Zurich, Sonneggstrasse 5, 8092 Zurich, Switzerland*

³*Institute of Geochemistry and Petrology, ETH Zurich, Clausiusstrasse 25, 8092 Zurich, Switzerland*

The giant impact hypothesis for Moon formation^{1,2} successfully explains the dynamic properties of the Earth-Moon system but remains challenged by the similarity of isotopic fingerprints of the terrestrial and lunar mantles³. Moreover, recent geochemical evidence suggests that the Earth’s mantle preserves ancient (or “primordial”) heterogeneity^{4,5} that predates the Moon-forming giant impact⁶. Using a new hydrodynamical method⁷, we here show that Moon-forming giant impacts lead to a stratified starting condition for the evolution of the terrestrial mantle. The upper layer of the Earth is compositionally similar to the disk, out of which the Moon evolves, whereas the lower layer preserves proto-Earth characteristics. As long as this predicted compositional stratification can at least partially be preserved over the subsequent billions of years of Earth mantle convection, the compositional similarity between the Moon and the accessible Earth’s mantle is a natural outcome of realistic and high-

probability Moon-forming impact scenarios⁸. The preservation of primordial heterogeneity in the modern Earth not only reconciles geochemical constraints^{4,5,9,10} but is also consistent with recent geophysical observations¹¹⁻¹⁴. Furthermore, for significant preservation of a proto-Earth reservoir, the bulk composition of the Earth-Moon system may be systematically shifted towards chondritic values.

As the only planet in our solar system, the Earth is orbited by a single and massive moon. The leading theory for the formation of the Earth-Moon system with its high angular momentum involves a giant impact followed by lunar aggregation from the impact debris disk¹. The canonical giant impact model involves a graze-and-merge impact, in which a Mars-sized body (or “Theia”) collides with the proto-Earth at an oblique angle at roughly the escape velocity of the system². In this model, however, Theia contributes a larger fraction of silicates (~70% by mass) to the proto-lunar disk than to the proto-Earth. Unless Theia and the proto-Earth had almost the same isotopic composition, this imbalance is at odds with the strong isotopic similarity of the Earth’s and lunar mantles, e.g., in terms of oxygen¹⁵ and titanium¹⁶.

One way to reconcile this compositional similarity involves the post-impact re-equilibration of the Earth and the Moon-forming disk¹⁷. This model, however, is unable to explain the isotopic similarity of the Earth and Moon in highly refractory elements, for example, titanium¹⁶. More recently, several alternative giant-impact models have been proposed. A near equal-mass “Sub-Earth” impact¹⁸ or the disruption of a fast-spinning Earth (close to self-breakup) by a small impactor¹⁹ can indeed explain the isotopic similarity. However, the proposed solutions are low-

probability events: equal-mass collisions are highly unlikely in the late stage of planetary accretion⁸, and planetary embryos hardly reach spins that are close to self-breakup in hydrodynamic simulations²⁰. Both models also predict an angular momentum that is too high for the early Earth-Moon system, and the mechanisms proposed to remove the excess angular momentum exclusively work in a narrow tidal parameter range²¹. Alternatively, multiple-impact models have been suggested for lunar origin²⁰, certainly broadening the favourable parameter space compared to single-impact models, and giving rise to mixing through mergers of moonlets with different isotopic composition. However, the dynamics of moonlets are highly uncertain, and primitive moonlets might be lost during repeated impacts pre-dating the Moon-forming stage²².

Here, we explore the mixing state of the Earth-Moon system in low-velocity, low-angular-momentum impact scenarios. We consider the canonical model² and the hit-and-run model²³ (see Figure 1a, for these $v_{imp} < 1.3v_{esc}$, where v_{imp} is the impact velocity and v_{esc} is the escape speed), which are both high-probability impact configurations²⁴ and lead result naturally in the current angular momentum of the Earth-Moon system. We apply a new hydrodynamical Lagrangian method: Meshless Finite Mass (MFM) (see Methods subsection 2). This method is better at capturing fluid mixing and at resolving the core-mantle boundary than the widely-used smoothed-particle hydrodynamical approach⁷.

In our simulations of such impacts, a strong shock propagates almost perpendicular to the line connecting the centers of the two impacting bodies after the first contact. In both the canonical and hit-and-run scenarios, the part of the impactor that can avoid direct collision is sheared into

a spiral structure which, shortly afterwards, collapses into clumps. The clumps re-impact the highly distorted target to eject some additional target material into the circum-planetary debris disk (Supplementary Video; Figure 1b). Figure 1c shows the predicted fraction of target material in the post-impact body, F_{tar} as a function of normalized enclosed mass (which corresponds to the radius, within which a given planetary mass fraction is enclosed). Even though mixing is more efficient with our new method than in previous studies, most of the impactor’s silicates still remain in the outer layer of the post-impact target mantle (low F_{tar}). This prediction is explained by inefficient transfer of angular momentum during the impact (Methods subsection 1). Focused shock heating in the outer layer (Supplementary Video) results in a steep entropy profile (Figure 1d) through most of the mantle. In particular, there is a distinct entropy jump at radius R , or at a normalized enclosed mass of $\sim 0.7 M_{\oplus}$. In terms of mass, this R corresponds to ~ 1000 km depth in the present-day mantle.

For the metal core, our models also predict a steep entropy and compositional profile in the aftermath of the impact. The entropy of the deep core even drops below its initial condition of 1200 J/kg/K. This is well explained by the effects of phase transitions near the core-mantle boundary, which can be captured by the MFM method, and results in a redistribution of energy, and entropy, from the core to the mantle⁷(Methods subsection 2, Extended Data Fig. 2, 6). The impactor’s metal mostly remains near the top of the core. Depending on the conditions of metal-silicate (impactor metallic core/target silicate mantle) equilibration, this prediction may provide an explanation for the ~ 300 -km-thick compositionally stratified layer that is seismically observed at the top of the present-day outer core²⁵.

To test our model predictions with geochemical observations, we estimate the unknown compositions of the impactor's (Theia) and target's (proto Earth) mantles from the known isotopic compositions of the accessible part of the Earth's mantle and Moon¹⁵ (See Supplementary material for calculation using alternative data). Figure 2a shows the allowed $\Delta^{17}\text{O}$ -difference as a function of the mass of the mantle that remains poorly homogenized (or preserved) over the age of the Earth. If the present-day mantle is fully homogenized such that any primordial stratification is completely removed, a common assumption in previous studies, Theia and the proto-Earth must have been rather similar in composition. For example, only 30 ppm $\Delta^{17}\text{O}$ difference between parent bodies are allowed in our best canonical model (run 5). On the other hand, if the assumption of full homogenization is relaxed, and the predicted mantle stratification can be (partially) preserved through the present day, larger compositional differences can be reconciled with the available data. For example, considering the preservation of a compositionally-distinct domain below R , differences of up to 54 ppm (run 13) in $\Delta^{17}\text{O}$ are allowed (Figure 2b), particularly for the hit-and-run models, which display larger fractions of proto-Earth silicate material in the disk than the canonical models (table 1; Figure 1). These large values are consistent with the compositional difference between potential parent bodies of the Earth-Moon system in N-body simulations of planetary accretion⁸. For realistic parent-body compositional differences²⁶, inefficient mixing of the Earth's mantle through time can indeed help to resolve the geochemical similarity of the accessible Earth mantle and Moon. Even for moderate mixing across R , our models can critically increase the allowed compositional difference between parent bodies (see Figure 2a).

Whether post-impact heterogeneity can persist through ~ 1 Myr of magma-ocean and ~ 4.5

Gyrs of mantle convection is controlled by the initial compositional and thermal profiles of the mantle. Our models predict the formation of a deep magma ocean due to the energy release of the giant impact²⁷ (see Extended Data Fig. 6). While major-element compositions of the post-impact mantle layers above and below R depend on the unknown bulk compositions of Theia and the proto-Earth, respectively, an enrichment of the lower (proto-Earth) layer in FeO and SiO₂ is generally consistent with the evolving of physical conditions of multi-stage core formation during progressive planetary accretion^{28,29}. Furthermore, FeO-enrichment of the deep proto-Earth's mantle may have been promoted by compositional fractionation (and subsequent overturn)³⁰ during any magma-ocean episode(s) that predate(s) the Moon-forming impact. Even just a slight FeO-enrichment of the lower layer is sufficient to promote stable stratification through various magma-ocean stages. A long lasting stratification should be favoured by the entropy gradient across the post-impact mantle predicted by our models as the observed sub-adiabatic entropy gradient should prevent redistribution by convection.

After the final magma-ocean episode that follows the giant impact, mixing during long-term solid-state mantle convection is controlled by the density and viscosity contrasts between the two layers. Primordial heterogeneity can survive mantle stirring as blobs over a range of spatial scales (meters to terameters)^{31,32}. Intrinsically high densities and viscosities of the primordial deep-mantle layer as sustained by an enrichment in FeO and SiO₂ of the proto-Earth's mantle (see above) impede efficient mixing across R . For example, ref. ²⁸ predicts a molar Mg/Si of ~ 0.98 for the proto-Earth's (lower) mantle, corresponding to a predominant abundance of the high-viscosity mineral bridgmanite (Mg,Fe)SiO₃, implying poor mixing. While some degree of whole-mantle mixing

is indicated by the sinking of a subset of subducted slabs of oceanic lithosphere through the entire mantle, the stagnation of other slab segments¹¹ and the deflection of upwelling plumes¹² at ~ 1000 km depth (i.e. about radius R) is indeed consistent with restricted mixing. Sharp seismic-velocity contrasts at similar depths support this interpretation, and provide direct evidence for large-scale compositional mantle heterogeneity^{13,14}. The preservation of primordial noble gases¹⁰, e.g. the large missing budget of argon⁹, provides complementary evidence for incomplete homogenization of primordial mantle reservoirs. ^{182}W isotopic evidence^{4,5} requires that least a subset of the preserved heterogeneity predates the moon-forming impact, and thus reflects proto-Earth compositions.

According to our results, the preservation of a significant fraction of primordial mantle heterogeneity through the age of the Earth can explain the isotopic similarity between the Earth's and lunar mantles for a relatively wide range of parent-body compositional differences (Figure 2). Preservation of SiO_2 -enriched heterogeneity further helps to balance the bulk-Earth's silica budget relative to the chondritic compositional range. Future geochemical and geophysical studies of lower-mantle composition will contribute to constrain the chemistry and origin of Earth's parent bodies, and thus, ultimately, of the inner solar nebula, providing the means to test effectively our scenario.

Methods

Estimation of the penetration depth of the impactor's silicates. In the gravity dominated regime, the interaction between the impactor's mantle and the target's mantle behaves like a fluid collision.

One fluid element can only deliver half its momentum/angular momentum to a roughly equal mass fluid element due to the completely inelastic nature of a fluid collision. The transport of angular momentum through shock waves, primarily the contact shock at their first contact, is also inefficient because the shock is almost symmetric to the line of centres. The impactor’s mantle keeps roughly half its initial angular momentum, $0.35(1 - \gamma)L_{imp}$ (confirmed by our simulations), so that it cannot sink deep into the target’s mantle. To avoid rotational instability, the specific angular momentum of the post-impact target must not decrease as radius increases (Rayleighs criterion); in simulations, the outer part rotates faster. In the best possible case, we assume the impactor’s silicates concentrate in a thin shell and they rotate with materials from the target’s mantle, residing outside the shell, at constant specific angular momentum (Extended Data Fig. 1). The materials beyond the shell contain the rest of the angular momentum, $(0.65 + 0.35\gamma)L_{imp}$. Even for $\gamma = 0.15$, the impactor’s mantle cannot penetrate half the target’s mantle. A hit-and-run collision is more complicated due to interaction with the escaping part and stronger oblique shocks, but the angular momentum transport is still inefficient with R a little deeper (see table 1).

Simulations and analysis. We simulate the giant impacts using the GIZMO code³³, which is a descendant of the GADGET code³⁴ and its SPH method widely used in previous impact simulations). GIZMO indeed contains the legacy SPH implementation of the GADGET code, newer SPH implementations such as PSPH, and, most importantly the novel Meshless Finite Mass (MFM). Gravity is coupled to all these different hydro methods using the same treecode scheme³³. The MFM method is an improved hydrodynamics formulation that is fundamentally different from the Smoothed Particle Hydrodynamics (SPH). GIZMO MFM does effective volume partition accord-

ing to the particle distribution and then solves the Riemann problem to update the fluid variables and can be regarded as a generalized moving mesh method. It employs no explicit artificial viscosity and thus shows better conservation property than SPH³⁵. MFM captures shocks and subsonic turbulence in giant impact simulations accurately, so it can simulate the mixing properly⁷. We use about 500K particles in our simulations, which is comparable to present-day high resolution simulations. We run a 2M particles simulation as a convergence test (Extended Data Fig. 2). A comparison between the standard SPH simulation, which suppresses mixing, and MFM simulation is presented in Extended Data Fig. 3.

We apply the ANEOS/M-ANEOS equation of state^{36,37} with iron comprising the core and dunite comprising the mantle. We build the initial condition for planets (30 wt% iron, 70 wt% dunite) by solving the hydrodynamic equilibrium with an isentropic profile and place the particles (computational elements) in spherical shells to represent the equilibrium profile³⁸. The temperature on the planet surface is about 2000K, corresponding to an entropy of 2700 J/kg/K in the mantle and 1200 J/kg/K in the core. We run a comparison study with higher initial entropy and our results are robust concerning the initial entropy value (Extended Data Fig. 4). Note that the same version of ANEOS/M-ANEOS is implemented in SPH and MFM, so that any difference that we observe between simulations carried out with these two methods will only stem from the underlying hydrodynamical solver.

We characterize the modeled impacts by determining the disk mass/angular momentum, the predicted Moon mass, planet mass/angular momentum and the internal structure of the post-impact target. The former is done following a standard approach, i.e., bounded particles with periapsis

distance larger than the equatorial radius of the planet are classified as disk particles^{20,39}. This calculation is preformed at least 40 hours after the impact, i.e. when the system saturates to a quasi-steady state³⁹ (Extended Data Fig. 5). We calculate the entropy profile by arithmetically averaging the entropy across spherical shells (assuming spherical symmetry). The fraction of materials from the target is calculated analogously. The iron core is slightly oblique with an equatorial radius that is slightly ($< 5\%$) larger than the polar radius; hence, the profiles is not messed up at the core-mantle boundary. A counter-intuitive result involves that that core entropy can drop below its initial value for MFM, as shown by the entropy profile (e.g., Figure 1d).

This prediction by our MFM models contrasts with that of our SPH models (Extended Data Fig. 3). The entropy drop in the core for MFM is caused by a phase transition and the associated redistribution of internal energy, and entropy, from the core to the mantle, hence it has a physical origin⁷. Indeed, as the outer core, near the core-mantle boundary, melts first, entropy locally increases, forcing the inner core to decrease its own entropy in order to maintain thermodynamical equilibrium. This entropy loss outweighs the entropy gain through shocks in the central core region. In contrast, in SPH simulations, the core and mantle are separated by an artificial tensional force^{7,40,41} (see also Extended Data Fig. 6). This force largely isolates the core, causing the core to evolve nearly adiabatically⁷. The physical heating associated with shocks is somewhat overestimated by the usage of artificial viscosity^{7,34}; as a result, the entropy slightly increases in the core for SPH. That the entropy in the central core does not decrease for SPH, is thus mostly due to a numerical artifact. The marked difference between MFM and SPH, i.e. in terms of the temperature and entropy distribution near the core-mantle boundary, is visualized in Extended Data

Fig. 6.

Code availability The latest version of the GIZMO code is made available by its author, Philip Hopkins at <http://www.tapir.caltech.edu/~phopkins/Site/GIZMO.html>

Data availability The data files that support our analysis will be made available upon reasonable request.

Acknowledgements We thank Martin Jutzi, Prasenjit Saha, Romain Teyssier and Qing-Zhu Yin for stimulating discussions. We acknowledge support from the Swiss National Science Foundation via the NCCR PlanetS.

Contributions H.D. conceived the idea of linking the moon formation impact to the Earth mantle heterogeneity and planned the project. C.R. built the equation of state (EOS) library and F.B. prepared the EOS lookup table. H.D. and C.R. incorporated the EOS library into the hydrodynamical code and prepared the initial conditions. H.D. ran the simulations and did the visualisation and interpretation. C.R., L.M., J.S. also helped in the interpretation. M.B. and M.M. contributed to the geodynamic and cosmochemistry argument, respectively. H.D., M.B. and M.M. prepared the manuscript. L.M. reviewed the manuscript and all authors commented on it.

Competing Interests The authors declare that they have no competing financial interests.

Correspondence Correspondence and requests for materials should be addressed to H.D.(email:hp Deng@physik.uzh.ch)

1. Cameron, A. G. & Ward, W. R. The origin of the moon. In *Lunar and Planetary Science Conference*, vol. 7 (1976).
2. Canup, R. M. & Asphaug, E. Origin of the Moon in a giant impact near the end of the Earth's formation. *Nature* **412**, 708–712 (2001).
3. Asphaug, E. Impact origin of the moon? *Annual Review of Earth and Planetary Sciences* **42**, 551–578 (2014).
4. Rizo, H. *et al.* Preservation of earth-forming events in the tungsten isotopic composition of modern flood basalts. *Science* **352**, 809–812 (2016).
5. Mundl, A. *et al.* Tungsten-182 heterogeneity in modern ocean island basalts. *Science* **356**, 66–69 (2017).
6. Barboni, M. *et al.* Early formation of the moon 4.51 billion years ago. *Science advances* **3**, e1602365 (2017).
7. Deng, H. *et al.* Enhanced mixing in giant impact simulations with a new lagrangian method. *The Astrophysical Journal* **870**, 127 (2019).
8. Mastrobuono-Battisti, A. & Perets, H. B. The composition of solar system asteroids and earth/mars moons, and the earth–moon composition similarity. *Monthly Notices of the Royal Astronomical Society* **469**, 3597–3609 (2017).
9. Allègre, C. J., Hofmann, A. & O’Nions, K. The argon constraints on mantle structure. *Geophysical Research Letters* **23**, 3555–3557 (1996).

10. Mukhopadhyay, S. Early differentiation and volatile accretion recorded in deep-mantle neon and xenon. *Nature* **486**, 101–104 (2012).
11. Fukao, Y. & Obayashi, M. Subducted slabs stagnant above, penetrating through, and trapped below the 660 km discontinuity. *Journal of Geophysical Research: Solid Earth* **118**, 5920–5938 (2013).
12. French, S. W. & Romanowicz, B. Broad plumes rooted at the base of the earth's mantle beneath major hotspots. *Nature* **525**, 95 (2015).
13. Jenkins, J., Deuss, A. & Cottar, S. Converted phases from sharp 1000 km depth mid-mantle heterogeneity beneath western europe. *Earth and Planetary Science Letters* **459**, 196–207 (2017).
14. Waszek, L., Schmerr, N. C. & Ballmer, M. D. Global observations of reflectors in the mid-mantle with implications for mantle structure and dynamics. *Nature Communications* **9**, 385 (2018).
15. Herwartz, D., Pack, A., Friedrichs, B. & Bischoff, A. Identification of the giant impactor theia in lunar rocks. *Science* **344**, 1146–1150 (2014).
16. Zhang, J., Dauphas, N., Davis, A. M., Leya, I. & Fedkin, A. The proto-earth as a significant source of lunar material. *Nature Geoscience* **5**, 251 (2012).
17. Pahlevan, K. & Stevenson, D. J. Equilibration in the aftermath of the lunar-forming giant impact. *Earth and Planetary Science Letters* **262**, 438–449 (2007). [1012.5323](https://doi.org/10.1016/j.epsl.2007.08.011).

18. Canup, R. M. Forming a moon with an earth-like composition via a giant impact. *Science* **338**, 1052–1055 (2012).
19. Čuk, M. & Stewart, S. T. Making the moon from a fast-spinning earth: A giant impact followed by resonant despinning. *Science* **338**, 1047–1052 (2012).
20. Rufu, R., Aharonson, O. & Perets, H. B. A multiple-impact origin for the moon. *Nature Geoscience* **10**, 89–94 (2017).
21. Wisdom, J. & Tian, Z. Early evolution of the earth–moon system with a fast-spinning earth. *Icarus* **256**, 138–146 (2015).
22. Pahlevan, K. & Morbidelli, A. Collisionless encounters and the origin of the lunar inclination. *Nature* **527**, 492–494 (2015).
23. Reufer, A., Meier, M. M., Benz, W. & Wieler, R. A hit-and-run giant impact scenario. *Icarus* **221**, 296–299 (2012).
24. Jackson, A. P., Gabriel, T. S. & Asphaug, E. I. Constraints on the pre-impact orbits of solar system giant impactors. *Monthly Notices of the Royal Astronomical Society* (2017).
25. Helffrich, G. & Kaneshima, S. Outer-core compositional stratification from observed core wave speed profiles. *Nature* **468**, 807–810 (2010).
26. Dauphas, N. The isotopic nature of the earths accreting material through time. *Nature* **541**, 521–524 (2017).

27. Nakajima, M. & Stevenson, D. J. Melting and mixing states of the earth's mantle after the moon-forming impact. *Earth and Planetary Science Letters* **427**, 286–295 (2015).
28. Kaminski, E. & Javoy, M. A two-stage scenario for the formation of the earth's mantle and core. *Earth and Planetary Science Letters* **365**, 97–107 (2013).
29. Rubie, D. C. *et al.* Accretion and differentiation of the terrestrial planets with implications for the compositions of early-formed solar system bodies and accretion of water. *Icarus* **248**, 89–108 (2015).
30. Elkins-Tanton, L. T. Linked magma ocean solidification and atmospheric growth for earth and mars. *Earth and Planetary Science Letters* **271**, 181–191 (2008).
31. Manga, M. Mixing of heterogeneities in the mantle: effect of viscosity differences. *Geophysical Research Letters* **23**, 403–406 (1996).
32. Ballmer, M. D., Houser, C., Hernlund, J. W., Wentzcovitch, R. M. & Hirose, K. Persistence of strong silica-enriched domains in the earth's lower mantle. *Nature Geoscience* **10**, 236–240 (2017).
33. Hopkins, P. F. A new class of accurate, mesh-free hydrodynamic simulation methods. *Monthly Notices of the Royal Astronomical Society* **450**, 53–110 (2015).
34. Springel, V. The cosmological simulation code gadget-2. *Monthly notices of the royal astronomical society* **364**, 1105–1134 (2005).

35. Deng, H., Mayer, L. & Meru, F. Convergence of the critical cooling rate for protoplanetary disk fragmentation achieved: The key role of numerical dissipation of angular momentum. *The Astrophysical Journal* **847**, 43 (2017).
36. Thompson, S. & Lauson, H. Improvements in the chart d radiation-hydrodynamic code iii: Revised analytic equations of state. Tech. Rep., Sandia Labs. (1974).
37. Melosh, H. A hydrocode equation of state for sio2. *Meteoritics & Planetary Science* **42**, 2079–2098 (2007).
38. Reinhardt, C. & Stadel, J. Numerical aspects of giant impact simulations. *Monthly Notices of the Royal Astronomical Society* **467**, 4252–4263 (2017).
39. Canup, R. M., Barr, A. C. & Crawford, D. A. Lunar-forming impacts: High-resolution SPH and AMR-CTH simulations. *Icarus* **222**, 200–219 (2013).
40. Agertz, O. *et al.* Fundamental differences between SPH and grid methods. *Mon. Not. R. Astron. Soc.* **380**, 963–978 (2007).
41. Hosono, N., Saitoh, T. R., Makino, J., Genda, H. & Ida, S. The giant impact simulations with density independent smoothed particle hydrodynamics. *Icarus* **271**, 131–157 (2016).
[arXiv:1602.00843v1](https://arxiv.org/abs/1602.00843v1).
42. Pierazzo, E., Vickery, A. & Melosh, H. A reevaluation of impact melt production. *Icarus* **127**, 408–423 (1997).

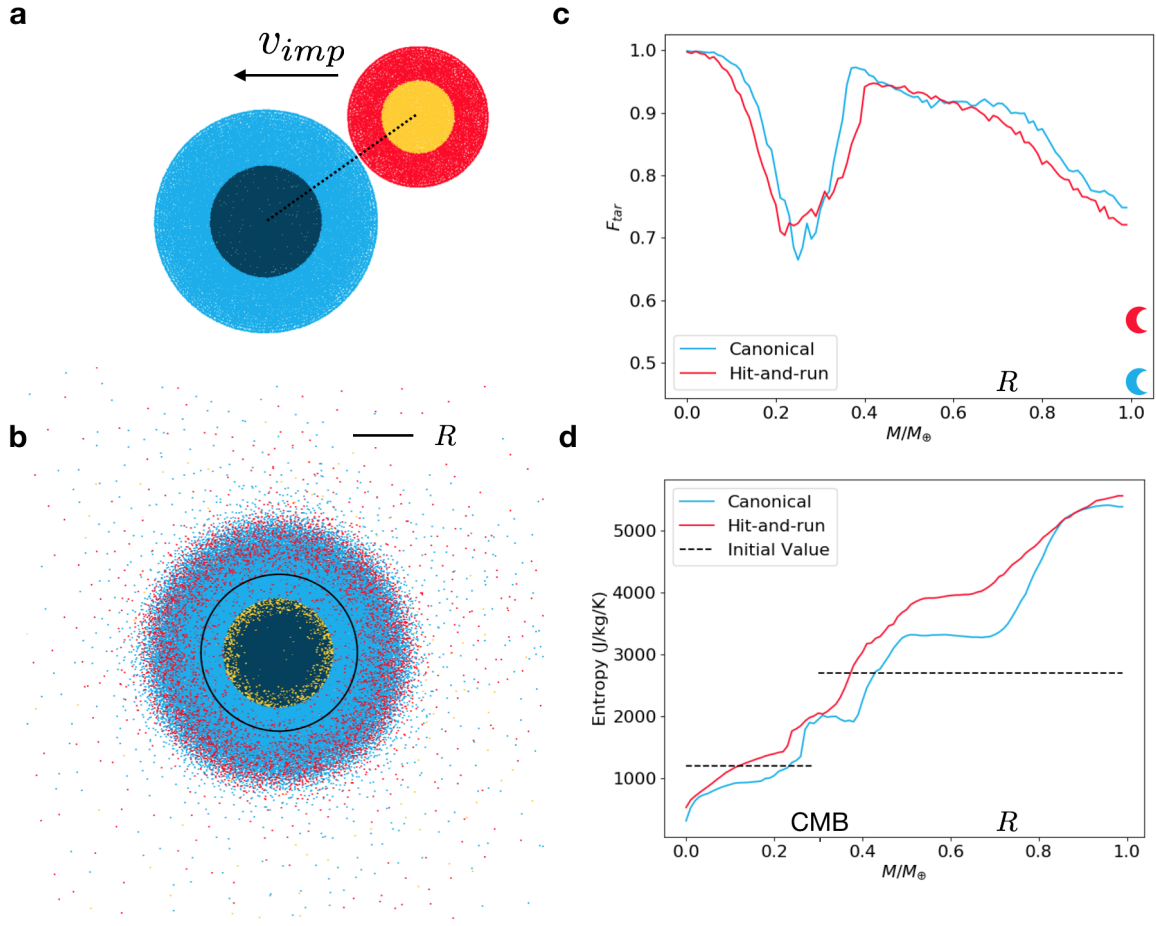


Figure 1: The internal structure of the post-impact Earth, after (i) canonical and (ii) hit-and-run collisions. **(a)** The initial condition just before the impact with the impactor's and target's mantle/core as marked with red/yellow and light-blue/dark-blue colors, respectively. The compositional structure of the post-impact target is visualized as **(b)** a 2D cross-section through the 3D model for run 13, and **(c)** 1D average profiles for runs 5 (canonical, blue) and 13 (hit-and-run, red). The average composition of the disk is denoted by a half-moon symbol. Panel **d** shows the related entropy profiles with black dash lines indicating the initial condition. A significant entropy jump is predicted at a radius R (i.e., at a normalized enclosed mass of $\sim 0.7M_{\oplus}$), corresponding to a kink in the compositional profile.

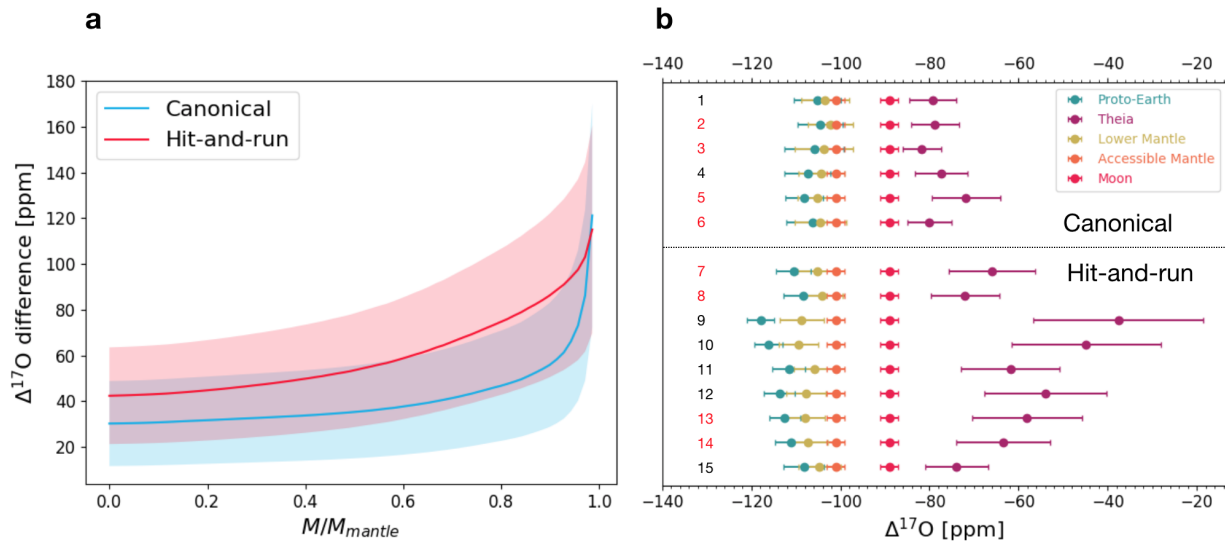


Figure 2: The oxygen isotopic composition of all reservoirs involved in the collision. Using the compositional profiles predicted by our models, we calculate the compositions of the lower-mantle layer, Theia and proto-Earth based on those of the accessible present-day mantle and Moon¹⁵. Panel **a** shows the allowed $\Delta^{17}\text{O}$ difference between Theia and the proto-Earth for runs 5 (blue) and 13 (red) as a function of the mass of the reservoir that remains unmixed with the accessible mantle. The shaded regions/error bars correspond to 1σ SEM uncertainty¹⁵. Panel **b** shows the estimated $\Delta^{17}\text{O}$ for all reservoirs and all runs (table 1) assuming that no mixing occurs in the Earth’s mantle across R (i.e., mass of the unmixed reservoir is $\sim 50\%$ of that of the mantle). For example, Theia’s oxygen isotopic composition could have been up to 54 ppm higher than that of the proto-Earth for run 13, simultaneously resulting in an isotopic difference between the accessible and lower mantle of 7 ppm. See Supplementary Material for details, as well as plots for elements Ti and Cr.

Table 1: Parameters and results of impact simulations

Run	M_{tar}	M_{imp}	b	$\frac{v_{imp}}{v_{esc}}$	$\frac{L_F}{L_{EM}}$	$\frac{L_D}{L_{EM}}$	$\frac{M_D}{M_L}$	$\frac{M_{planet}}{M_E}$	$\frac{M_U}{M_{mantle}}$	$F_{U,tar}$	$F_{D,tar}$	$\frac{M_{Fe}}{M_D}$	$\frac{M_M}{M_L}$
1	0.85	0.12	0.71	1.00	0.91	0.16	0.87	0.94	0.46	0.84	0.38	0.16	0.73
2	0.85	0.12	0.73	1.00	1.18	0.35	1.48	0.95	0.50	0.86	0.40	0.04	1.48
3	0.85	0.16	0.71	1.00	1.30	0.32	1.70	0.98	0.49	0.80	0.30	0.04	1.5
4	0.85	0.16	0.73	1.00	1.30	0.23	1.22	0.98	0.43	0.79	0.39	0.12	1.08
5	0.90	0.16	0.71	1.00	1.32	0.32	1.98	1.0	0.52	0.81	0.47	0.01	1.19
6	0.90	0.16	0.73	1.00	1.53	0.38	1.64	1.0	0.52	0.80	0.34	0.05	1.64
7	0.85	0.2	0.574	1.20	1.33	0.29	1.63	0.99	0.59	0.79	0.52	0.08	1.26
8	0.85	0.2	0.574	1.25	1.26	0.26	1.45	0.98	0.62	0.80	0.47	0.09	1.14
9	0.90	0.2	0.537	1.20	1.30	0.05	0.30	1.06	0.55	0.79	0.64	0.01	0.20
10	0.90	0.2	0.537	1.25	1.32	0.13	0.81	1.04	0.60	0.79	0.62	0.03	0.48
11	0.90	0.2	0.537	1.30	1.30	0.20	1.20	1.04	0.54	0.79	0.55	0.12	0.79
12	0.90	0.2	0.574	1.15	1.38	0.14	0.88	1.04	0.54	0.79	0.59	0.01	0.51
13	0.90	0.2	0.574	1.20	1.34	0.23	1.23	1.02	0.56	0.79	0.57	0.08	1.07
14	0.90	0.2	0.574	1.25	1.30	0.24	1.30	1.02	0.59	0.80	0.54	0.09	1.30
15	0.90	0.2	0.574	1.30	1.20	0.23	1.18	1.02	0.50	0.79	0.44	0.16	1.18

At the end of each run (at least 40 hours after the impact, until no clumps present in the disk) we evaluate the proto-lunar disk and the post-impact target compositions following an established approach^{20,39} (see Methods subsection 2). The canonical (top) and hit-and-run (bottom) models are separated by the horizontal dashed line. $M_E, M_L, M_D, M_M, M_{planet}$ are the real masses of the Earth and Moon, and the predicted masses of the proto-lunar disk, the formed moon, and post-impact target (formed Earth), respectively. We also calculated the mass fraction of the mantle that lies beyond R , i.e., $\frac{M_U}{M_{mantle}}$. The fraction of target's silicates in the upper layer mantle ($r > R$) is denoted as $F_{U,tar}$. Runs with $M_M > 1.0M_L$ and $M_{Fe}/M_D < 0.1$ are regarded as successful impacts and highlighted with the red color¹⁹.

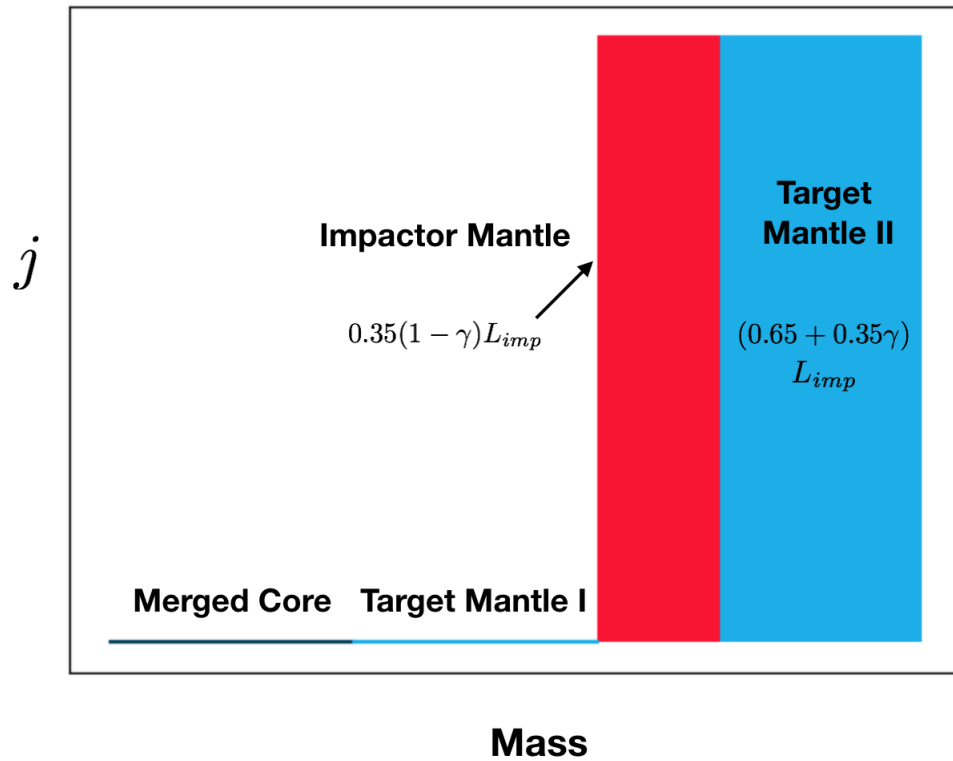


Figure 3: **Extended data figure 1:** An idealized model to estimate the maximum possible penetration depth. The specific angular momentum profile, which must not decrease with radius to avoid rotational instability, is just a step function. The silicate materials can be placed outside the impactor's silicates are less than those inside the impactor's silicates, thus smaller than half the target mantle's mass for an impact with $\gamma < 0.15$.

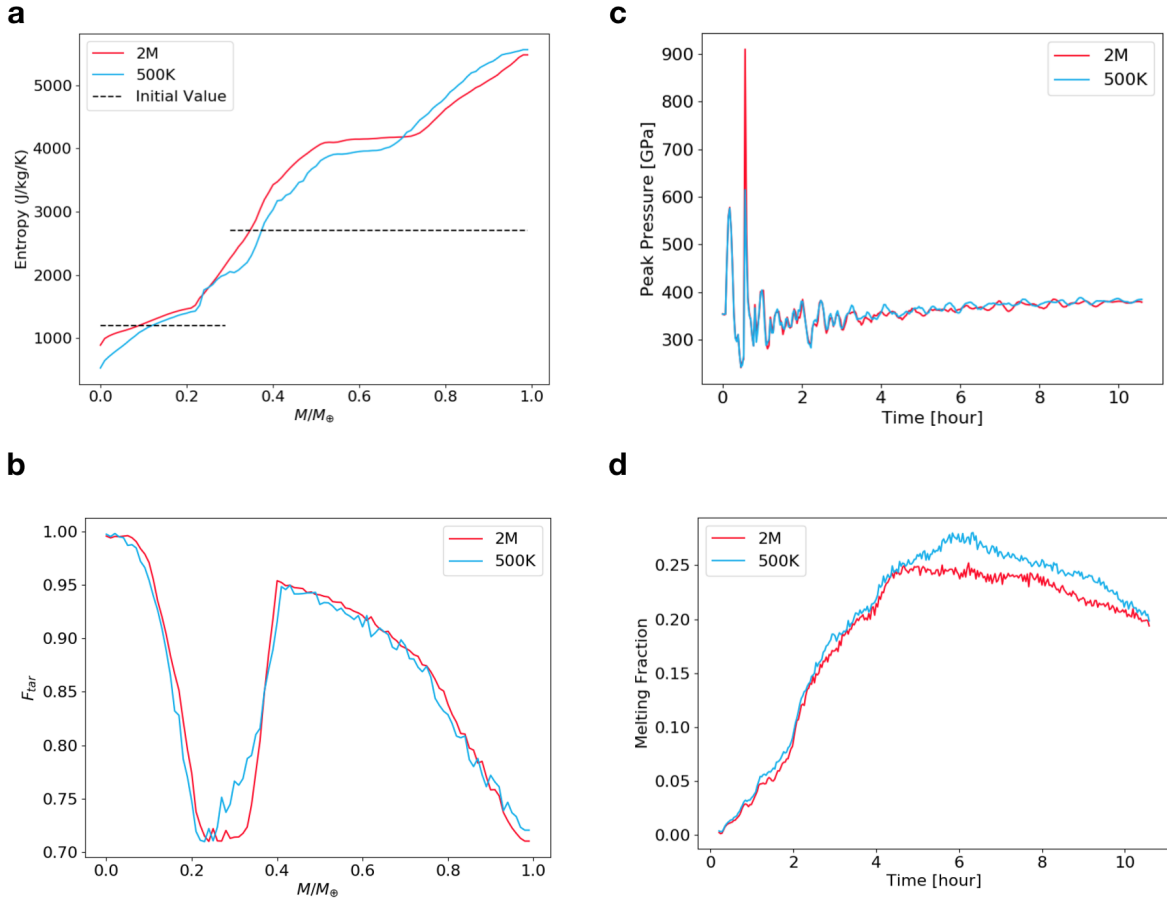


Figure 4: **Extended data figure 2:** Resolution test of our MFM simulations in terms of number of particles. A high-resolution case with 2M particles (and otherwise the same parameters as run 13) indeed numerically converges well with run 13. Even though small differences persist in terms of the details of the **(a)** entropy profile, **(c)** peak pressure and **(d)** melt fraction of the core⁴², the most critical model prediction (i.e., **(b)** the compositional profile) converges well at the two resolutions shown. The pressure fluctuation is stronger in the lower resolution simulation (due to larger discretization noise), which leads to exaggerated melt fraction in the core.

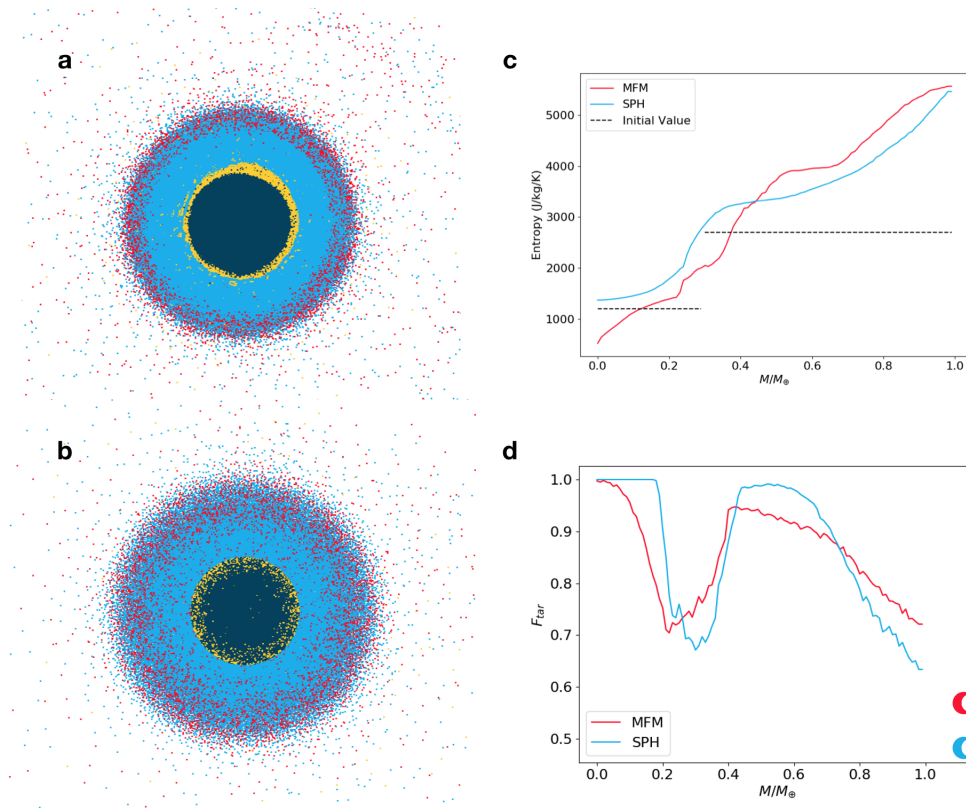


Figure 5: **Extended data figure 3:** Comparison between MFM and standard SPH simulation of run 13 in table 1. **a** and **b** show the material distribution in the post-impact target in the SPH and MFM run respectively. Compared to MFM, impactor materials tend to be enhanced near the planet's surface and near to top of the core in SPH, and nearly absent in the deep mantle and core⁷. **c** The entropy profile for both methods. The entropy jump in the mantle is sharper for MFM than for SPH. In the MFM simulations, the entropy drop in the core is explained by transfer of energy due to the phase transition at the core-mantle boundary⁷ (Extended data figure 6). **d** The mass fraction of materials from the target is plotted as a function of the normalized enclosed mass. Mixing of impactor material with the deep target mantle and core is more efficient for MFM than for SPH. For a detailed discussion in terms of the comparison of both approaches, we refer the reader to ⁷.

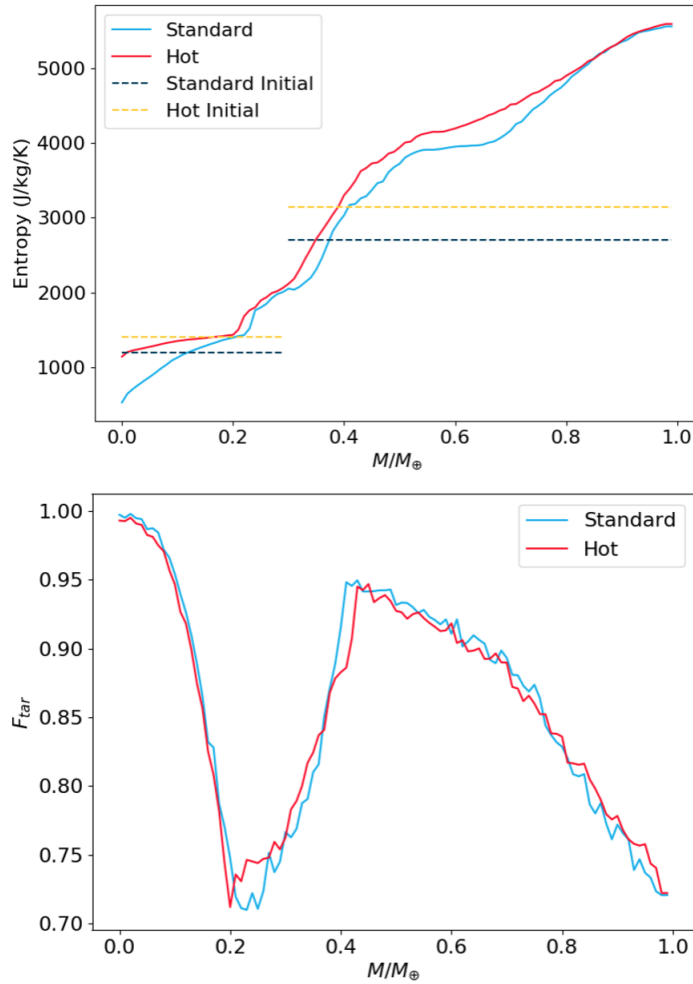


Figure 6: **Extended data figure 4** Model results as a function of initial condition. The upper and lower panels shows the final entropy and compositional profiles, respectively, for run 13 (blue), and an analogous case with a higher initial entropy target (1400 J/kg/K for iron and 3200 J/kg/K for dunite) (red). In the case with an initially hotter target, the entropy jump in the mantle is slightly less sharp than for run 13. However, the compositional profile is robust, remaining virtually unchanged. The disk mass and angular momentum also remain robust with differences $<2\%$.

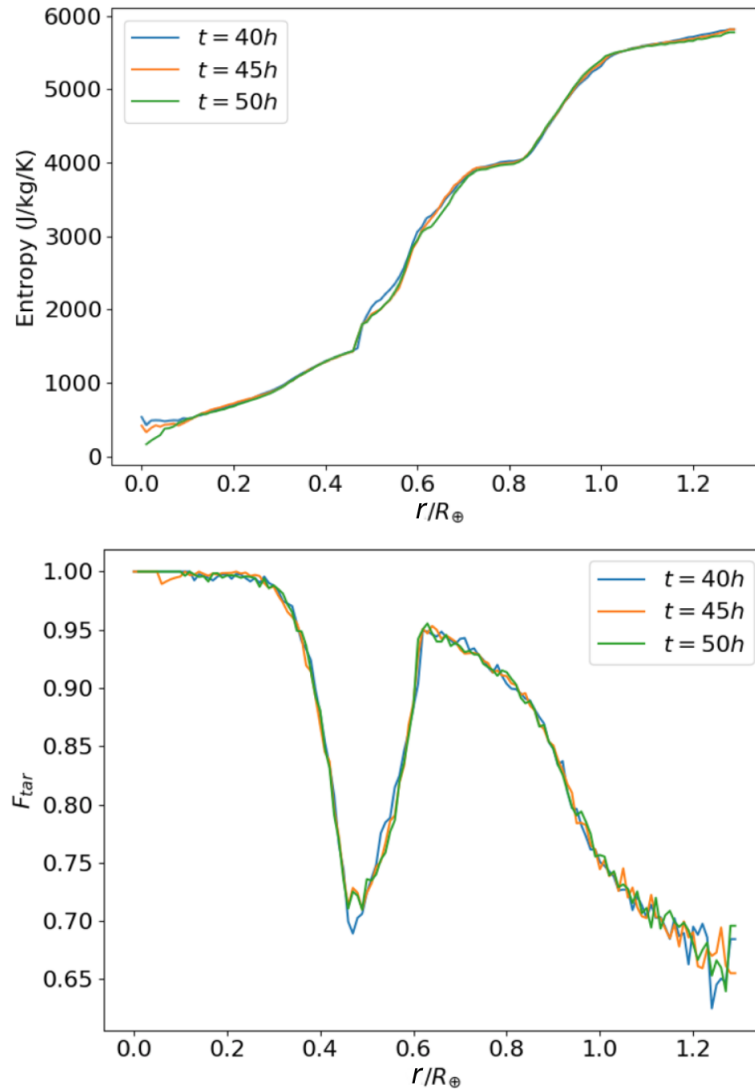


Figure 7: **Extended data figure 5** The saturation of the thermal and compositional state of the post-impact target. The upper and lower panels display the entropy and compositional profiles, respectively, at different model times for run 13. After 40 hours, the post-impact target already has reached a stable state. This result confirms that our approach of performing the analysis at ≥ 40 hours after the impact is reliable. Here is the movie for [run 13](#) (note the code time unit is 1.77 h).

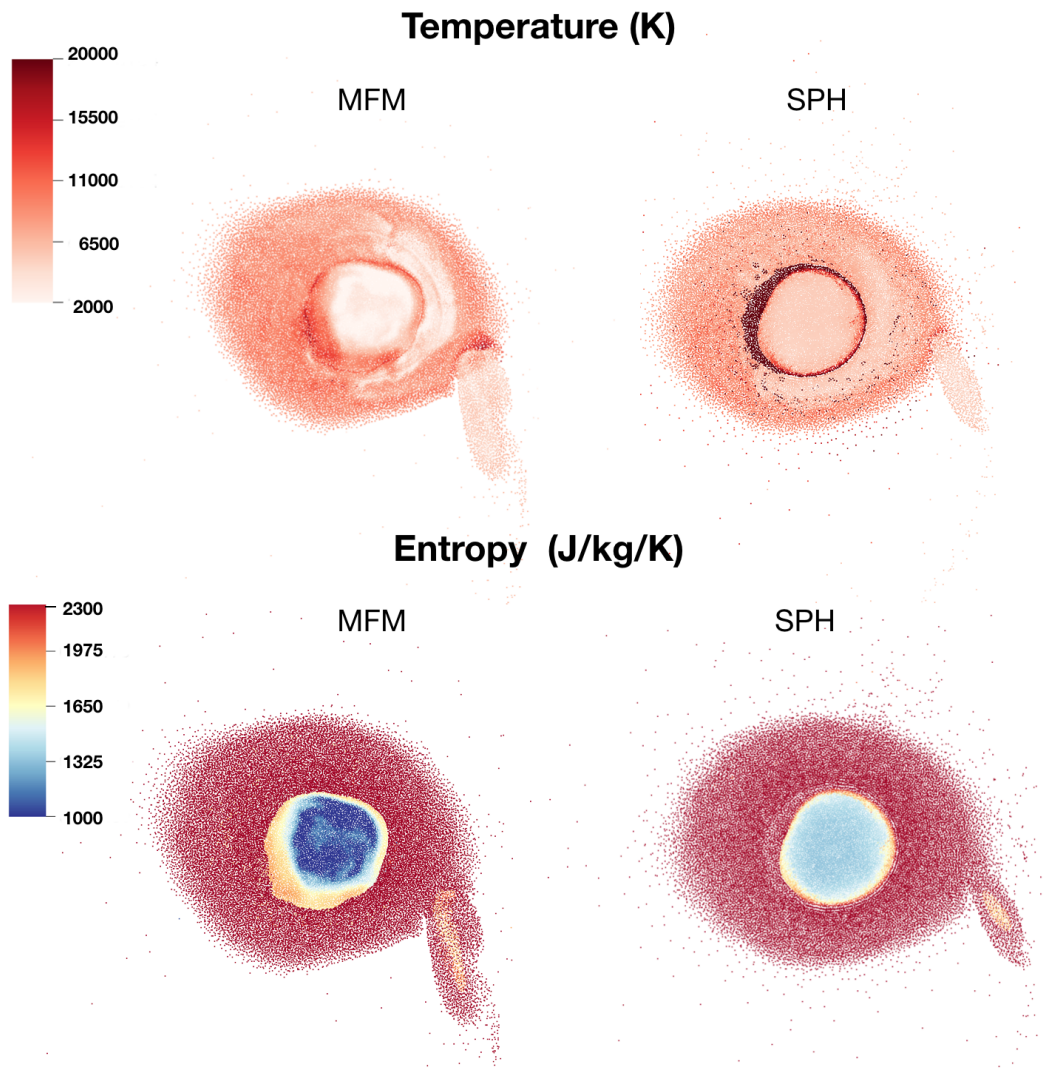


Figure 8: **Extended data figure 6** The difference of the thermal state in MFM and SPH. We show snapshots of the SPH and MFM comparison run at 7.08 hours. There is a clear separation between the core and mantle in the SPH simulation due to numeric issues⁷; the temperature difference across the core-mantle boundary can be larger than 10000K.

Supplementary Material

Determination of the correlated ranges of inferred isotopic compositions of the proto-Earth, Theia, and the Lower Mantle.

In the following, these letters / subscripts denote material derived from the respective reservoirs:

P = Proto-Earth
E = Earth (bulk)
T = Theia (the impactor)
U = Earth's Upper Layer Mantle
L = Earth's Lower Layer Mantle
M = Moon (bulk), or the Moon-forming disk
J = Ejecta (leaving the Earth-Moon system)

Also, X is the isotopic composition of a reservoir (e.g., expressed in permil deviation from a standard), m the mass of a reservoir, and f the fractional mass of the target (= the proto-Earth in Giant Impact settings) mantle in the reservoir.

All equations below will use the basic mass balance equation, where two reservoirs of mass m_1 and m_2 , and isotopic compositions of X_1 and X_2 , are merged into a new reservoir of mass $m_t = m_1 + m_2$ and composition X_t . X_t is then:

$$X_t = [m_1 * X_1 + m_2 X_2] / m_t \quad (1)$$

Note that this assumes that the mass-fractions of the respective element (e.g., oxygen) are identical in all reservoirs. If that is not the case (e.g., if the proto-Earth's mantle contains 40% O, while Theia's mantle contains 45% O), then in the following, X_i should be treated as the product of the mass-fraction c_i (e.g., 40%) and the actual isotopic composition X'_i : $X_i = c_i * X'_i$.

We start with the assumption that both the proto-Earth and Theia are initially well-mixed, so that their silicate mantles can be treated as a single reservoir. In classical Giant Impact mass-balance calculations, one would fully mix these two reservoirs, with the respective contributions f_E , f_M determined previously by the SPH simulations, to arrive at the resulting bulk isotopic composition of Earth and Moon. The mass-balance calculation for the isotopic composition of (the silicate part of) the Earth is:

$$X_E = [m_{P,E} * X_P + m_{T,E} * X_T] / m_E \quad (2)$$

So, $m_{P,E}$ is the total mass of the proto-Earth mantle material that ends up in the Earth's mantle, while m_E is the mass of the Earth's mantle. For convenience, we can also define:

$$f_i = m_{P,i} / m_i \quad (3)$$

so that f_i is the fraction of proto-Earth mantle material in the respective reservoir (i). Since the rest of the mass of the reservoir must come from Theia ($m_{P,i} + m_{T,i} = m_i$) we can also set:

$$m_{T,i} = (1 - f_i) * m_i \quad (4)$$

We can then re-write equation (2) as:

$$X_E = f_E * X_P + (1 - f_E) * X_T \quad (5)$$

Similarly, we can formulate the same equation for the Moon:

$$X_M = f_M * X_P + (1 - f_M) * X_T \quad (6)$$

Here, f_M represents the fraction of proto-Earth mantle material in the Moon. The fact that f_E and f_M (and thus X_E and X_M ; all other values must be the same) have been found to be different in SPH simulations of the Giant Impact, while X_E and X_M have been measured to be identical within uncertainty, is sometimes called the “isotopic conundrum” of the Moon’s formation.

In the paper, we show that a Giant Impact simulated with an updated SPH model will result in a stratified Earth mantle, where the upper mantle contains a smaller fraction of proto-Earth material than the lower mantle, although the proto-Earth fractions of the upper mantle and the disk (from which the Moon forms) are similar. The composition of the three reservoirs is then:

$$X_M = [m_{P,M} * X_P + m_{T,M} * X_T] / m_M \quad (7)$$

$$X_U = [m_{P,U} * X_P + m_{T,U} * X_T] / m_U \quad (8)$$

$$X_L = [m_{P,L} * X_P + m_{T,L} * X_T] / m_L \quad (9)$$

There is a fourth reservoir, which contains ejecta, material ejected from the Earth-Moon-system back into a heliocentric orbit. For canonical impacts, this reservoir has masses between 0.001 and 0.02 Earth masses, while for hit-and-run impacts, the masses are considerably larger, between 0.04 and 0.07 Earth masses. For simplicity, we will assume that for canonical impacts, the contribution from the proto-Earth is zero, while for hit-and-run impacts, the proto-Earth contribution is typically on the order of 30%. The mass-balance equation for the ejecta reservoir is:

$$X_J = [m_{P,J} * X_P + m_{T,J} * X_T] / m_J \quad (10)$$

As for the “simple” case of the fully mixed post-Giant-Impact Earth (equations 5 and 6), we can again express the $m_{P,i}$ and $m_{T,i}$ variables using the respective contribution from the proto-Earth:

$$X_M = f_M * X_P + (1 - f_M) * X_T \quad (11)$$

$$X_U = f_U * X_P + (1 - f_U) * X_T \quad (12)$$

$$X_L = f_L * X_P + (1 - f_L) * X_T \quad (13)$$

$$X_J = f_J * X_P + (1 - f_J) * X_T \quad (14)$$

Since we do know the isotopic composition of the Moon (X_M) and the upper mantle (X_U) as well as the masses and/or proto-Earth contributions in all reservoirs (from the SPH simulations; m_i and/or f_i), we are left with four unknown variables (X_P , X_T , X_L , X_J) and four equations relating them. We

use equations (11) and (12) to solve for X_P and X_T , which are then in turn used to calculate X_L and X_J using (13) and (14).

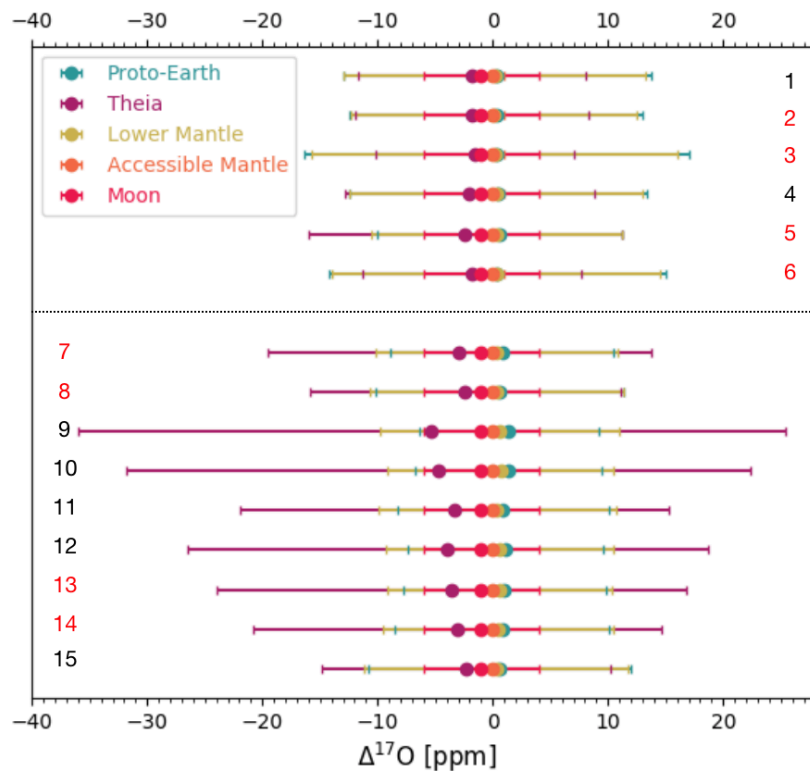
$$X_T = [f_U * X_M - f_M * X_U] / [f_U * (1 - f_M) - f_M * (1 - f_U)] \quad (15)$$

$$X_P = [X_M - (1 - f_M) * X_T] / f_M \quad (16)$$

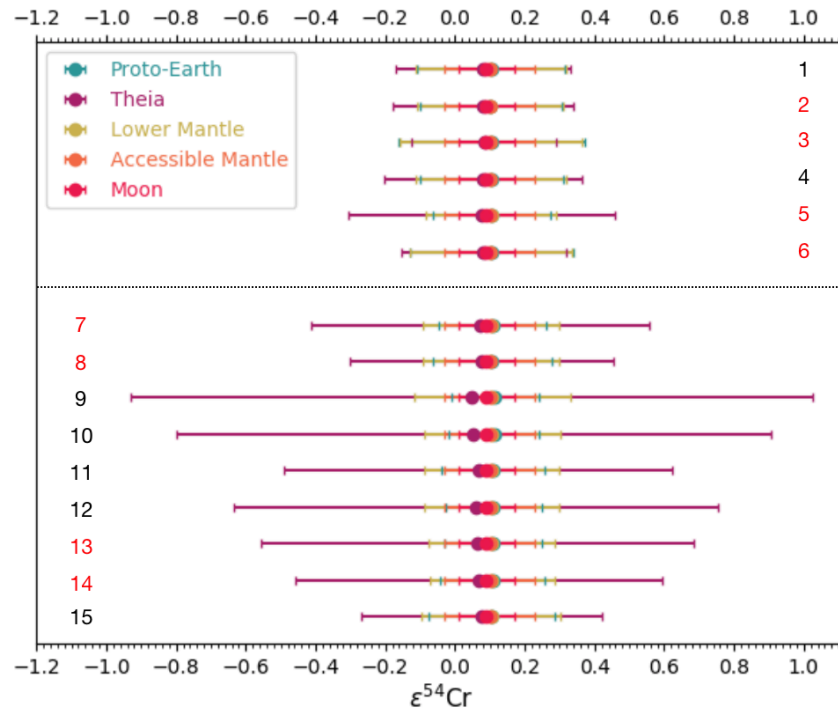
These equations were then used to create Fig.2.

The stated uncertainties of the isotopic compositions of the different reservoirs (e.g., Theia, proto-Earth, etc.) are estimated by using the maximal difference in O isotopic composition (from Herwartz et al., 2014) allowed between the Earth ($\Delta^{17}O = -0.101 \pm 0.002\text{‰}$) and Moon ($-0.089 \pm 0.002\text{‰}$) within the respective uncertainties, i.e., -0.103‰ for the Earth and -0.087‰ for the Moon, and then determining the difference to the nominal value. This conservative approach tends to overestimate the uncertainties.

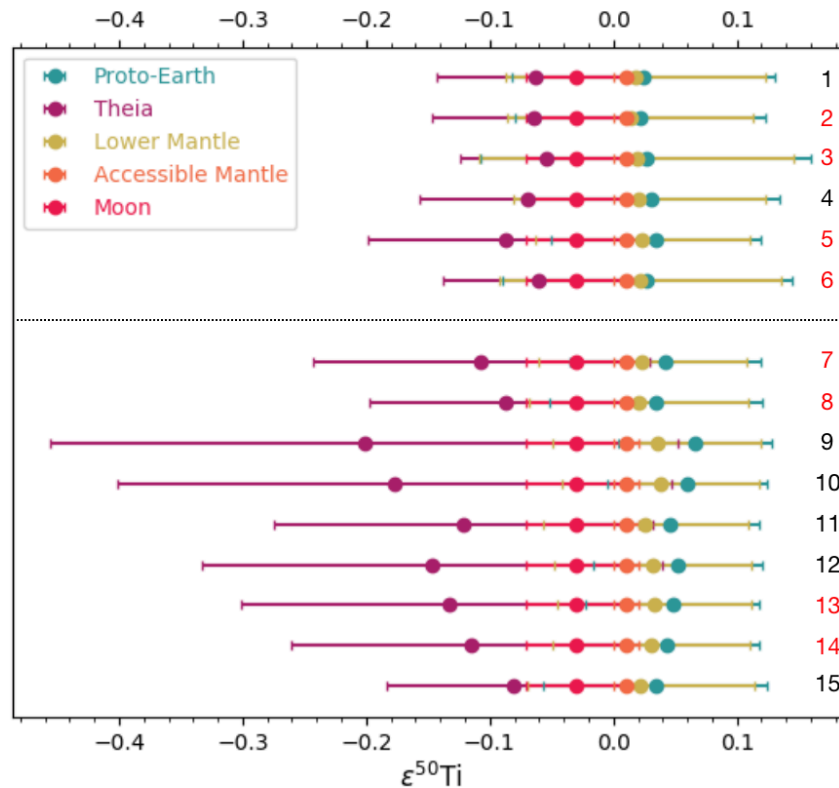
Supplementary figure 1. The same as fig 2b but using data from Young et al., 2016 and the error bar shows 2 SEM uncertainty. The measured difference of oxygen isotope composition in the Earth-Moon system is mainly due to the different samples (Young 2016) and Young et al. 2016 has one sample shows even larger oxygen difference between Earth and Moon than Herwartz et al., 2014.



Supplementary figure 2. The same figure as fig 2b but for Cr using Mougél et al. 2018



Supplementary figure 3. The same figure as fig 2b but for Ti using Zhang et al. 2012.



References

- [1] Mougél, B., Moynier, F. & Göpel, C. Chromium isotopic homogeneity between the moon, the earth, and enstatite chondrites. *Earth and Planetary Science Letters* 481, 1–8 (2018).
- [2] Herwartz, D., Pack, A., Friedrichs, B. & Bischoff, A. Identification of the giant impactor theia in lunar rocks. *Science* 344, 1146–1150 (2014).
- [3] Zhang, J., Dauphas, N., Davis, A. M., Leya, I. & Fedkin, A. The proto-earth as a significant source of lunar material. *Nature Geoscience* 5, 251 (2012).
- [4] Young, E. D. *et al.* Oxygen isotopic evidence for vigorous mixing during the moon-forming giant impact. *Science* 351, 493–496 (2016).
- [5] Meier, M. M., Reufer, A. & Wieler, R. On the origin and composition of theia: Constraints from new models of the giant impact. *Icarus* 242, 316–328 (2014).

Remarks on the core entropy and EOS

We have published a series of tests of the reliability of MFM in a technical paper (Deng et al. 2019 ApJ, hereafter paper1). Among other things, this paper shows that the entropy drop is caused by phase transitions and the associated internal energy redistribution.

We would first like to point out that the code we use here, GIZMO (Hopkins 2017) is a multi-method code, including both SPH (widely used in impact simulation) and MFM (first applied by our group for impact simulations in paper1 and in this manuscript). In this framework MFM and SPH do share the same EOS implementation; so the difference found between these two numerical methods in the manuscript, especially in terms of the entropy difference, can only be caused by differences in the hydrodynamical methods.

The differences between the two methods that are relevant for our discussion are:

- First, traditional SPH suffers from spurious pressure forces at contact discontinuities (Agertz et al. 2007). In impact simulations, these forces may separate the mantle and core to some extent. - Second, SPH imposes artificial viscosity to capture shocks, which can result in excessive dissipation and suppress subsonic turbulence (for our case affecting mixing in the post-impact body), see e.g., Bauer & Springel 2012.

MFM is a relatively new method which does not suffer from the above two shortcomings, as they has been thoroughly shown in published papers describing the GIZMO code. For example, we note that MFM successfully passes benchmark tests such as the Kelvin-Helmholtz instability and forced subsonic turbulence test (sections 4.4.1 and 4.4.4 in Hopkins, 2015), which deal exactly with the two shortcomings described above. These capabilities of MFM are inherited from the fact that it solves the hydro equations in conservative form using an accurate Riemann solver and employing all the machinery of state-of-the-art finite volume 2nd order Godunov codes.

As a result of its more accurate representation of fluid flow as we describe below (see also paper1), MFM can resolve the energy flux related to phase changes under certain circumstances. We show that this flux is related to a physical process and not an artifact (although maybe under-resolved, see below). **Most importantly, we show that our main results (i.e. post-impact compositional profiles across the Earth's mantle and core) remain robust irrespective of this energy flux or resolution.**

In paper1, we run tests concerning the conservation of entropy. For summary see the table below:

	Tillotson typical core, ~1200J/kg/K	ANEOS/M-ANEOS typical core, 1200J/kg/K	ANEOS/M-ANEOS molten core, 1860J/kg/K
SPH	<i>entropy conserved</i>	<i>entropy conserved</i>	<i>entropy conserved</i>
MFM	entropy conserved, paper1 figure 10	entropy NOT conserved, pa- per1 figure 10	entropy conserved, paper1 figure 9

First, we perform an adiabatic expansion test: turning off gravity and letting the 0.89 Earth mass target expand freely. Entropy conservation is excellent in both SPH and MFM, validating our EOS implementation (see also the square test and the shock capturing test in paper1 appendix A). For example, the entropy of the core remains 1200J/kg/K even after 50 hours when the target expands 50 times in radius. (see paper1 figure 8, pressure release melting is isentropic)

In impact simulations, the target's core experiences expansion (not free/adiabatic expansion however) and compression constantly. We introduce the oscillation test to mimic the expansion and compression during the impact: a 0.89 Earth-mass proto-Earth model with an initial radial expansion velocity 1km/s at radius >0.7 Earth radius. The planet oscillates radially, and this makes a clean test to examine the entropy change without shock heating (note: the oscillations are subsonic). We take the entropy conservation of the core as an example in the following discussion.

The entropy in the SPH simulations is conserved with an error proportional to the amount of numerical dissipation introduced by artificial viscosity (paper1 figure 11). For the SPH oscillation simulation with ANEOS/M-ANEOS, we observe indeed an increase in the entropy of the core at the center. The oscillations are slow and no shocks are present. Artificial viscosity can be triggered for convergent flow (in the center during compression), which in this case leads to an internal energy/entropy gain. In Deng et al. (2017) we have shown that this is an issue in modelling accurately the evolution of self-gravitating disks, the issue being instead absent in MFM. That said, the entropy of the core is roughly conserved with no regions entering a low-entropy state.

MFM conserves entropy throughout the oscillation test with Tillotson EOS similarly to SPH, with the core oscillating along the same isentrope (paper1 figure 10, blue curve). We note that Tillotson EOS does not include phase transitions while ANEOS/M-ANEOS can model phase transitions (Brundage 2013). The default ANEOS library does contain a melting curve for iron (Prof. Gareth Collins, personal communication), and many previous studies used entropy >1650 J/kg/K as a simple criterion to identify molten iron in ANEOS (see, e.g., Pierazzo et al. 1977). We carried out one oscillation simulation with a fully molten core (core entropy 1860J/kg/K, planet surface ~ 10000 K) using MFM and again the entropy of the core is well conserved (paper1 figure 9). MFM conserves entropy provided that no phase transitions are present (absent in the EOS or the physical process). *Entropy conservation for MFM is even better than in SPH, as expected due to the absence of artificial viscous dissipation.*

When the initial core entropy is 1200 J/kg/K (planet surface ~ 2000 K, center ~ 4000 K as generally assumed in the Moon forming impact) the core entropy is not conserved in the MFM oscillation test. Such a model has a core initially close to the solidus (e.g., Alf et al. 1999). When such a proto-Earth oscillates, pressure release (decompression) melting starts at the outer core during expansion; the outer core is more susceptible to melting than the inner core because of the slope of the melting curve. As quasi pressure equilibrium is always maintained, the re-establishment of this equilibrium is associated with an energy redistribution towards the molten layer (note this is not heat conduction) (paper1, figure 10 right panel). The total related energy flux ignoring the source term of the gravitational energy is $\vec{\nabla}(\rho u + 0.5\rho v^2 + P)$ (Hopkins 2015). As a result, in order to maintain the same pressure the melt region near the CMB ought to have higher internal energy than solid iron under the same pressure (paper1 figure 10, right panel). During subsequent compression, the high internal energy molten region (this manuscript figure 8) redistributes energy towards the mantle. Thus, through consecutive expansion-compression cycles, the melt region act as an agent to redistribute energy from the inner core toward the core-mantle boundary, and eventually into the mantle.

In impact simulations, the constant decompression and compression cycles lead to a hot molten outer core (this manuscript figure 8) and thermal energy extraction from the central core. In the CTH (a well tested finite volume grid-based code) simulation of the canonical moon formation impact, the entropy of the core also drops when the same ANEOS EOS as here is used (paper1 figure 12). Similar internal energy redistribution can happen in the mantle. Thus, the energy flux out of the core is related to a physical process, and not an artifact. In turn, the fact that the entropy is conserved in SPH during phase transitions is a numerical artifact. That the energy flux is related to melting near the core-mantle boundary is further supported by full conservation of entropy in the case with an initially molten core (see above). **We acknowledge that achieving a quantitatively converged thermal state in general, and for the energy flux in particular, is challenging, and will likely require higher resolution than used here (not possible for a parameter study), because low resolution leads to strong oscillations (poor force resolution), more melting and more energy extraction from the core (this manuscript figure 4). We stress, however, that our conclusions remain robust as the compositional profile remains virtually unaffected by changes in resolution (this manuscript figure 4) or in the initial thermal state (this manuscript figure 6). While these changes affect the entropy profile (see above), they do not affect the compositional profile.**

Future studies with DISPH (e.g., Hosono et al 2015) using the ANEOS library will shed further light on the entropy drop in the centre core. We expect it to be in line with MFM as in the ideal gas simulations (Saitoh & Makino 2016). The cooling core may also be a pure artifact caused by the treatment of phase transitions in ANEOS which is far from realistic (Dr. Kai Wünnemann, private communication). In all, reevaluation of the reliability/accuracy of giant impact modelling should be taken seriously.

The figure below, which corresponds the MFM simulations in Extended data fig 6, shows that the outer core is indeed molten according to the ANEOS melting criterion (purple line). When it is compressed, it will not give back all the internal energy it gains from the inner core (second law of thermodynamics), but it releases some of it to the mantle. As a result, the inner core entropy eventually drops.

